Time-Resolved Absorption in Cryogenic and Room-Temperature, Direct-Drive Implosions

Introduction

Absorption of laser light in laser inertial confinement fusion (ICF) implosion experiments[1–4] is of pre-eminent importance since it provides the energy input. Current ICF implosions are scaled from future ignition experiments with thermonuclear gain and typically require laser pulses of complex temporal shape. These pulse shapes are chosen—among other considerations—to minimize the growth of hydrodynamic instabilities in the acceleration phase of the implosion.[5,6] They drive an optimized series of shock and compression waves that coalesce in the fuel and lead to hot-spot ignition, provided the fuel has been kept at a low adiabat α (α = minimum fuel pressure over Fermi-degenerate pressure).

An accurate understanding of the coupling of laser light to the target is essential for the success of implosion experiments. The laser light can be refracted, scattered, and absorbed. Hydrodynamic simulations are used to optimize the pulse shapes for specific target designs.[7–11] These simulations indicate that the scattered-light distribution in 60-beam implosion experiments is isotropic to within 1% or 2%. Experimental measurements of the laser light scattered into 4π strad are used to infer the absorption for comparison with hydrodynamic simulations.

Current implosion experiments on OMEGA are designed to study various parameters including the hydrodynamic stability of the implosion. The absorption of laser light crucially influences the hydrodynamics. All phases of laser absorption, refraction, and scattering in current experiments will be encountered in the early phases of future ignition experiments. Some potential problems of future ignition experiments cannot be fully investigated at present. The longer scale lengths that will be encountered in the future may favor nonlinear interaction processes beyond those in current implosion experiments[12] or dedicated long-scale-length planar interaction experiments.[13–16]

Time-integrated absorption measurements have been previously reported for direct-drive spherical target experiments.[2,4,17–21] Time-integrated measurements can mask dif-

ferences in the time evolution of the absorption that can lead to significant hydrodynamic consequences, such as shock mistiming and an increased adiabat of the inner shell surface of the imploding target. This article describes the experimental conditions, followed by examples of time-resolved scattered-light measurements in implosion experiments and a discussion of the underlying absorption processes. Conclusions are also presented.

Experimental Conditions

The OMEGA Laser System[22] operating with 60 UV beams (λ_L = 351 nm) irradiates cryogenic and room-temperature targets of ~860-μm diameter. Total laser energies are ≤24 kJ in laser pulses of ≤4 ns with shapes with or without 100-ps pickets ahead of the main pulse. The maximum overlapped irradiation intensity is 1.5×10^{15} W/cm^2. All beams are equipped with distributed phase plates (DPP's),[23–25] polarization smoothing (PS),[26] and smoothing by spectral dispersion (SSD)[27] in most experiments. The energy irradiation nonuniformity on target is <3% rms with each of the 60 beams slightly overfilling the target with ~5% energy spillover around the cold target. The intensity nonuniformity on target during the slowly varying parts of the pulse shape ranges between 3% and 7% when averaged over 200 to 300 ps. In the rapidly varying parts of the pulse shape the intensity nonuniformity is more difficult to quantify since it depends on pulse-shape irregularities, timing jitter among beams, and the precision and accuracy of the pulse-shape measurements for each beam. The intensity nonuniformity during the rapidly varying parts of the pulse shapes is estimated to be ≤15% rms.

The cryogenic targets[28] are plastic (CD) shells of ~860-μm diameter and 3- to 10-μm wall thickness filled with ~1000 atm of DT or D$_2$ and cooled and frozen into uniform,[29,30] ~100-μm solid DT or D$_2$ "ice" layers at ~18 K. The room-temperature targets are either CH or CD shells with walls of 10 to 40 μm filled with D$_2$ or DT gas (3 to 40 atm). The room-temperature targets are coated with ~100 nm of Al for gas retention. Gas diffusion at cryogenic temperatures is negligible and no Al coating is applied.

The principal diagnostic for determining laser absorption in these implosion experiments is provided by two full-aperture backscattering stations (FABS) located in beams 25 and 30.[4,18,31] Time-resolved scattered-light spectroscopy and time-integrated calorimetry in these stations are used to infer the absorption of light by the target. The absolutely calibrated FABS calorimeters provide cross-calibration for all time-resolved scattered-light spectra. A schematic of the diagnostic arrangement is shown in Fig. 113.36(a) along with typical time-resolved scattered-light spectra for a narrowband (no SSD bandwidth), 1-ns, room-temperature implosion.

There are four spectrally and time-resolved scattered-light–measurement channels[31] (one channel in each FABS and two channels located between focusing lenses). Two typical time-resolved scattered-light spectra are shown in Figs. 113.36(b) and 113.36(c) with no SSD bandwidth applied. The temporal resolution is ~80 ps and the spectral resolution is ~0.08 nm.

The calorimeters are calibrated using shots through the target chamber without a target, yielding absolute errors on the energy measurements of 1% to 3% at ~10 J into the focusing lenses of beam 25 or 30. The detection threshold for these calorimeters is ~0.04 J. For a typical 20-kJ implosion with ~50% absorption, this results in a calorimetry precision of ~1.5%. In the implosion experiments, the calorimeter measurements vary by 4% to 6%, leading to typical errors on the absorption of ~2% to 3%. These errors are about twice as large as expected but the source of these errors is not well understood at present. In addition to the FABS calorimeters, there are up to 17 scattered-light calorimeters located inside and outside of the target chamber. These calorimeters are cross-calibrated to the FABS calorimeters since absolute calibration of these calorimeters has proven to be very difficult to ascertain and maintain.

Near isotropy of the scattered light is predicted by hydrodynamic simulations. The schematic ray trace in Fig. 113.36(a) shows a variety of scattered ray paths that contribute to the FABS calorimeter and streak camera channels. This figure is greatly simplified as each point on each lens receives rays from many different directions and each FABS sees contributions from all 60 beams. The fractional contributions from each beam vary with time and beam. Since the FABS stations are in the line of sight of opposing beams, some light passes around the targets at early times [unshifted signal in Fig. 113.36(b)] and contributes to the FABS energy measurements. This "blow-by" is not isotropic and must be subtracted from the scattered-light measurements before the isotropically scattered-light energy
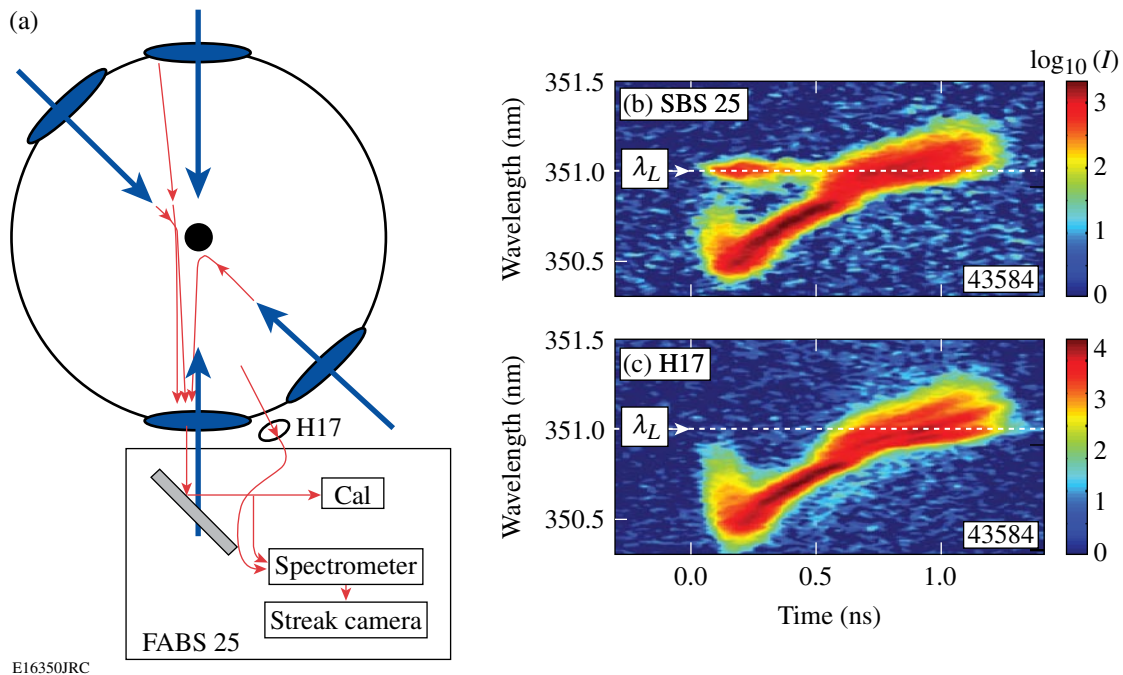

Figure 113.36
(a) Schematic of scattered-light diagnostics inside the OMEGA target chamber. The full-aperture backscatter station (FABS) is shown for beam 25 with its calorimeter and temporally and spectrally resolved backscatter channel. An additional channel for light scattered in between the focusing lenses is also shown (H17). Typical time-resolved backscatter spectra are shown in (b) for the FABS channel and (c) for the channel in between the focusing lenses for an imploding 20-μm-thick CH shell with DPP's and PS but no SSD bandwidth.

can be determined. This is done using target shots with only the beams opposing the two FABS stations. Since plasma formation on the limb of the target is minimal in this case, this measurement provides an upper limit of the blow-by. For consistency the two beams opposing the FABS can be turned off, which only minimally affects the FABS energy measurements for 58-beam shots but totally eliminates the need for blow-by corrections.

The two spectra shown in Fig. 113.36 clearly distinguish light that misses the target (blow-by) as it remains unshifted in wavelength [Fig. 113.36(b)]. For shots without beams opposing the FABS stations, the two spectra are practically indistinguishable. The time-resolved spectrum [Fig. 113.36(b)] allows for quantitative estimates of the blow-by, supporting the calorimetric estimates discussed above. The blow-by fraction depends on the pulse shape, pulse duration, and target and cannot be reasonably determined for all conditions. An estimated blow-by fraction of ~1.6% of the opposing beam energy is subtracted from the FABS calorimeter measurement to determine the diffusely scattered-light energy.

Results

Time-resolved scattered-light spectra are shown in Fig. 113.36 for a 1-ns square pulse implosion experiment and in Fig. 113.37(a) for an implosion using a complex pulse shape with 1-THz SSD bandwidth. The scattered-light power, obtained by integrating the spectra over the wavelength, is compared to predictions from hydrodynamic (*LILAC*[32]) simulations in Fig. 113.37(b). (Experimental time-resolved absorption fractions are not compared directly with simulations since the laser pulse shape and scattered-light spectra are recorded with different streak cameras and slight inaccuracies can lead to large errors upon division of one by the other.) To avoid the need for detailed blow-by corrections, the spectra taken in between the focusing lenses (e.g., H17) are used for most of the quantitative analyses. Two *LILAC* predictions for the scattered-light power are shown in Fig. 113.37(b), one for standard flux-limited electron-heat transport with $f = 0.06$ (Ref. 33) and the second using a nonlocal heat-transport model developed at LLE.[34,35] The differences between the experimental observations and the *LILAC* predictions apparent in Fig. 113.37(b) are typical for these experiments but the details differ depending on target and irradiation parameters.

The scattered-light spectra in Figs. 113.36 and 113.37 exhibit a similar rapid blue shift followed by a slow return to the initial laser wavelength and beyond. The spectra are modeled using ray-trace simulations based on density, velocity, and tempera-

ture profiles obtained from hydrodynamic (*LILAC*) simulations. Figure 113.38 shows schematically how all 60 beams of OMEGA contribute to the scattered light collected at any location. The contributions from each beam vary in time. The spectral shifts observed in Figs. 113.36 and 113.37 are due to the plasma evolution,[36] i.e., the temporally changing optical path length in the plasma traversed by any ray.
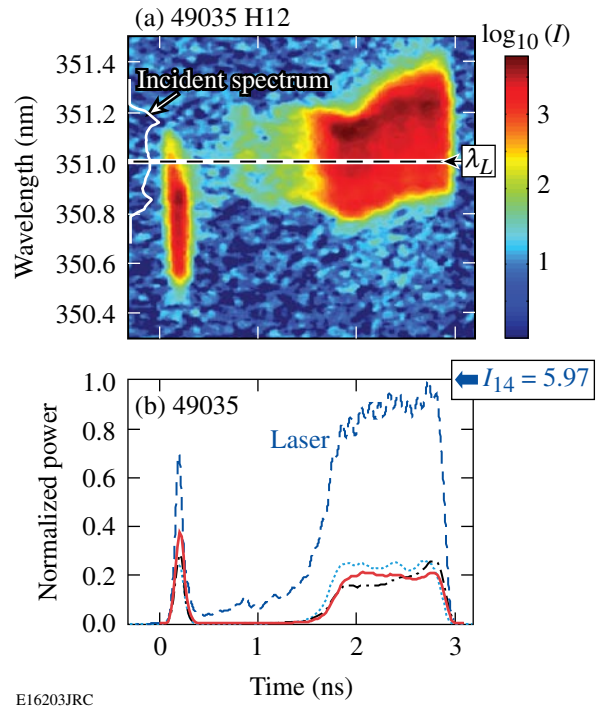

Figure 113.37

(a) Scattered-light spectrum and (b) incident and scattered-light powers for a cryogenic target (10-μm CH wall, 77-μm DT-ice layer, 858-μm diam) imploded with 17.7 kJ of fully smoothed laser energy (DPP's, PS, and 1-THz SSD bandwidth). The experimental scattered power is shown by the dotted line, the incident power by dashed lines, and *LILAC* predictions with nonlocal and flux-limited transport by solid and dashed–dotted lines, respectively.
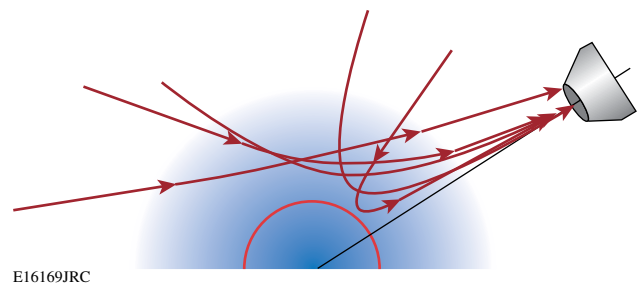

Figure 113.38

Illustration of scattered-light contributions from any of OMEGA's 60 beams to the light collected by a lens at the target chamber wall. The contributions from any one beam depend on both time and the position of the beam relative to the collector.

The experimental and simulated spectra are compared in Fig. 113.39 for a target irradiated with a 200-ps laser pulse without SSD corresponding to the picket shown in Fig. 113.37. For this narrowband experiment the anisotropic blow-by contribution to the scattered light observed in FABS25 is easily distinguished from the light that is isotropically scattered by the plasma. Simulations with the nonlocal electron-heat transport and the standard flux-limited transport are shown in Figs. 113.39(b) and 113.39(c) with Fig. 113.39(b) matching the experimental data better. The simulations include the blow-by around the target. The corresponding incident and scattered-light powers are shown in Fig. 113.40, where the blow-by has been removed from the spectrum. Excellent agreement between
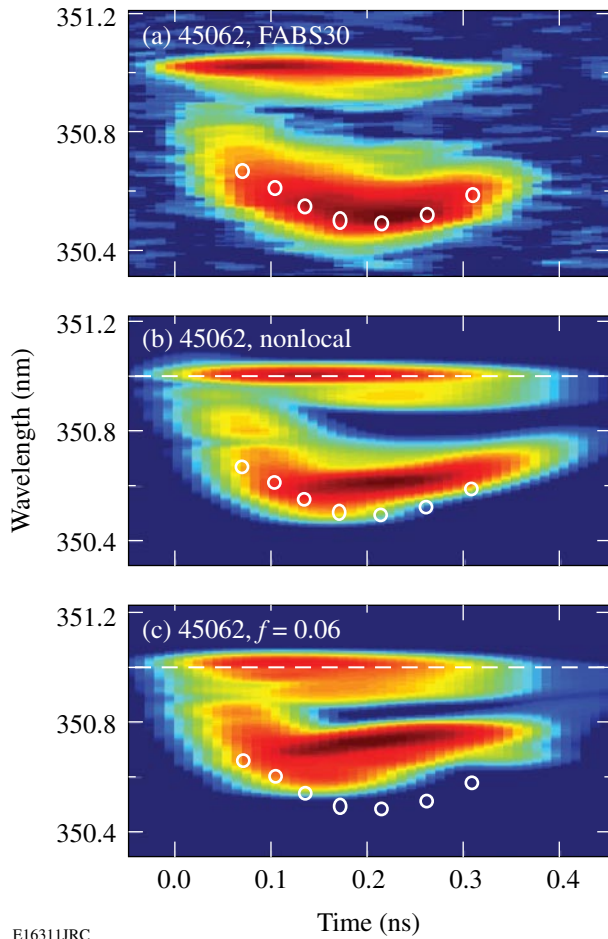
simulations using nonlocal transport and experimental data is apparent in this figure. The time-integrated absorption fraction for a number of 200-ps irradiation experiments is shown in Fig. 113.41. The agreement between the *LILAC* predictions using nonlocal transport is apparent from these figures, whereas the standard flux-limited transport significantly underestimates the absorption.
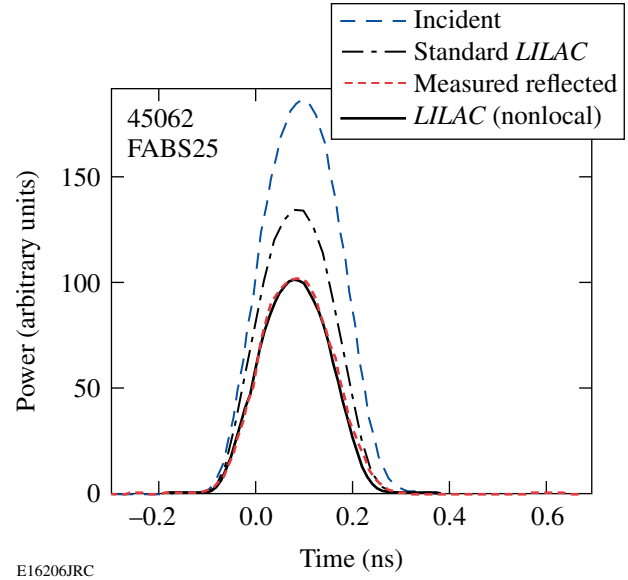

E16206JRC

Figure 113.40
Power histories of the incident and scattered light for the spectra shown in Fig. 113.39: the measured scattered-light power (short-dashed line), the incident power (long-dashed line), the predictions based on nonlocal transport (solid line), and standard *LILAC* predictions using flux-limited heat transport with $f = 0.06$ (dashed–dotted line).

E16311JRC

Figure 113.39
Time-resolved scattered-light spectra for a 200-ps spherical irradiation experiment of a warm 20-μm CH shell with DPP's and PS but no SSD bandwidth. The experimental spectrum is shown in (a) and two simulated spectra are shown in (b) and (c). Nonlocal electron-heat transport was used for the plasma parameters in (b) and standard flux-limited ($f = 0.06$) heat transport was used in (c). The white circles are added for easier comparison of the simulated spectra with the experimental spectrum.
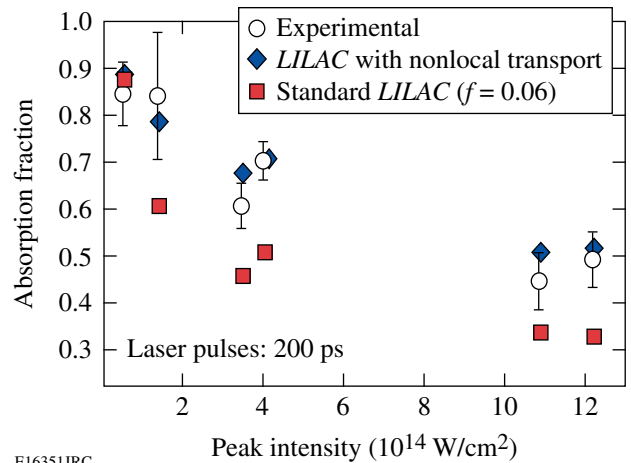

E16351JRC

Figure 113.41
The time-integrated absorption fractions for 200-ps irradiation experiments of CH targets (20-μm shells or solid spheres) with DPP's and PS. Most shots were without SSD bandwidth while two shots had 1-THz SSD bandwidth.

As shown in Fig. 113.37, hydrodynamic simulations using either flux-limited or nonlocal transport cannot accurately predict the scattered-light power at later times during the main part of the compression pulse ($t > 1.5$ ns in Fig. 113.37). A particularly striking example is shown in Fig. 113.42 where a warm plastic shell (20-μm CH wall, 873-μm diam) was imploded with a 1-ns square pulse, full beam smoothing, and 15.3-kJ laser energy. Instantaneously, the scattered-light spectra differ significantly from the incident spectrum as is evident from the lineouts in Fig. 113.42(a). The scattered-light power predicted by *LILAC* using constant flux-limited thermal transport significantly over-predicts the scattered power during the

first half of the pulse and then under-predicts it during the latter half. Simulations using nonlocal transport correctly estimate the scattered power during the first 150 ps but are consistently too low beyond that. The differences between the incident and scattered-light spectra [see lineouts in Fig. 113.42(a)] are indicative of a nonlinear interaction process as will be discussed on p. 43.

Another example of the measured and simulated scattered-light spectrum is shown in Fig. 113.43 for a cryogenic target implosion with a complex laser pulse designed to drive the target on a low fuel adiabat ($\alpha = 2$). Hydrodynamic simulations
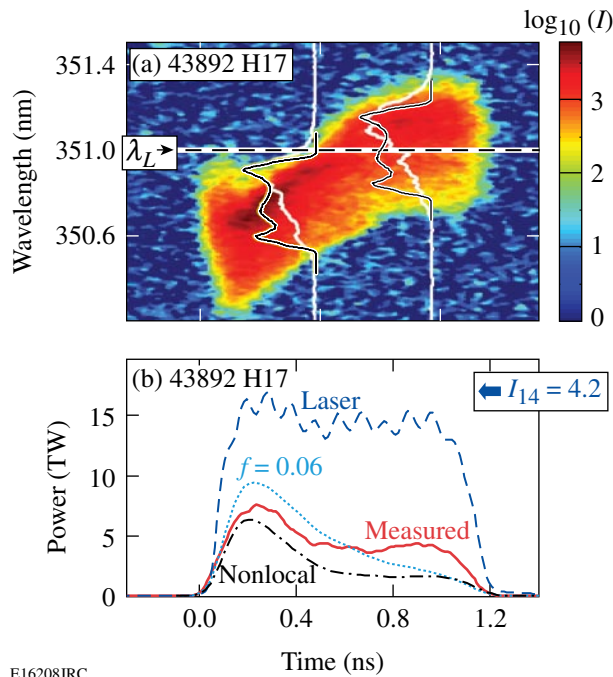

E16208JRC

Figure 113.42
(a) Scattered-light spectrum and (b) incident, measured, and predicted scattered-light powers for a room-temperature target (20-μm CH wall, 873-μm diam, 15 atm of D_2) imploded with a 1-ns laser pulse of 15.3-kJ energy with full beam smoothing (DPP's and PS, 1-THz SSD bandwidth). Lineouts of the spectrum shown in (a) are in white with the incident spectrum superposed in black-on-white. In (b) the measured scattered-light power is shown as a solid line, *LILAC* predictions using standard flux-limited electron transport with $f = 0.06$ are shown as a dotted line, and those with nonlocal transport are shown as a dashed–dotted line.
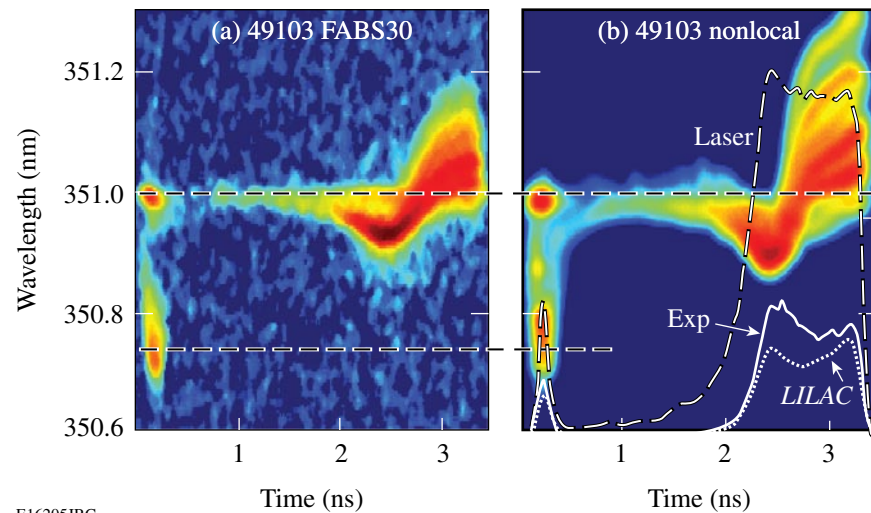

E16205JRC

Figure 113.43
(a) Measured and (b) simulated time-resolved scattered-light spectra for an imploding cryogenic target (10-μm CD wall, 95-μm D_2-ice layer, 855-μm diam) with 16 kJ of laser energy smoothed with DPP's and PS but no SSD bandwidth. The laser pulse shape is shown as white dashes in (b) along with the measured (solid white) and simulated (dotted white) scattered-light powers. The hydrodynamic simulations used nonlocal electron transport. (For details of comparison see the **Discussion** section, p. 43.)

with nonlocal transport were used to calculate the simulated spectrum [Fig. 113.43(b)]. The general shape of the simulated spectrum is close to that measured. The incident laser power is shown in Fig. 113.43(b) along with the measured and predicted scattered laser power.
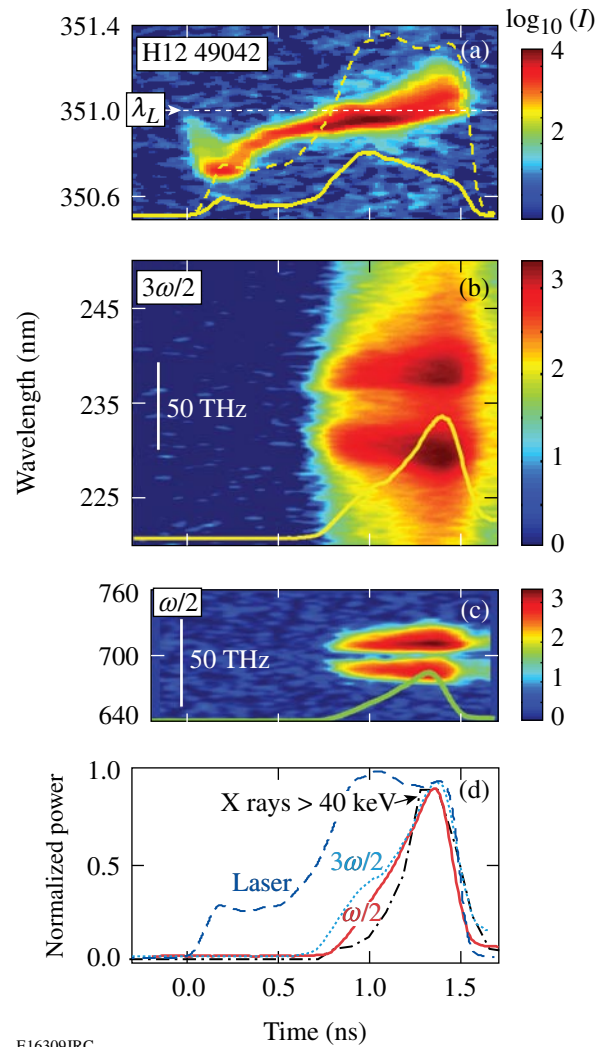
In addition to light scattered near the incident laser wavelength, laser light is scattered into half-harmonics ($\omega/2$ and $3\omega/2$) due to the two-plasmon-decay (TPD) instability. Stimulated Raman scattering (SRS)[37] has never been observed on OMEGA direct-drive-implosion experiments while half-harmonic spectra are regularly observed on OMEGA. The plasma waves produced by the TPD instability can generate energetic electrons leading to emission of hard x rays beyond 50 keV. Various scattered-light spectra and powers observed during a typical room-temperature implosion experiment are shown in Fig. 113.44. The wavelength scales of the half-harmonic spectra are chosen to have equal frequency (energy) scales for convenient comparison of the spectral features that are indicative of the TPD instability.

The half-harmonic and hard x-ray emission are superposed in Fig. 113.44(d). The power histories (two half-harmonics and hard x rays) are strikingly similar, suggesting their common TPD origin. Under well-controlled irradiation conditions (similar targets, same pulse shapes, but different intensities) the half-harmonic and hard x-ray signals exhibit an essentially identical exponential scaling with intensity (Fig. 113.45). An x-ray threshold around 4 to 5×10^{14} W/cm^2 is observed in Fig. 113.45. The half-harmonic emission has a threshold that is around 2×10^{14} W/cm^2, comparable to the theoretical threshold[38] as calculated for the average intensity in an equivalent linear density gradient for plane waves at normal incidence.

The intricate dependence of the TPD threshold to the density-gradient scale length (L_n), electron temperature (T_e), and intensity is seen in Fig. 113.46. A rough estimate for the TPD threshold is provided by the plane wave, linear-gradient-threshold parameter[38] $\alpha_{th} = I_{14} L_{n,\mu m} / 230\, T_{e,keV} > 1$, where I_{14} is the average intensity on target in units of 10^{14} W/cm^2. The laser burns through the plastic shell of this cryogenic target around the dip of the α_{th}-curve in Fig. 113.46(b). It should also be noted that the instantaneous peak intensities on target are typically $5\times$ larger than the average intensities.

Discussion

While time-integrated absorption measurements have been previously reported to be in good agreement with simulations,[4,21,39] the data presented here show the value of

Figure 113.44

Time-resolved scattered-light spectra for a room-temperature implosion using 25 kJ of laser energy with DPP and PS smoothing but no SSD bandwidth. [Target: plastic shell, 24-μm wall, outer 10 μm are doped with 6% (atomic) Si, filled with 15 atm of D$_2$.] The spectrum of the scattered light around the laser frequency and the incident and scattered power are shown in (a). In (b) and (c) the $3\omega/2$ and $\omega/2$ spectra and powers are shown on a common frequency (energy) scale. The normalized incident laser, odd-integer half-harmonic powers, and the time-resolved x-ray emission for $h\nu_x > 40$ keV are shown in (d).

time-resolved data since compensating differences between experimental data and predictions can lead to erroneous interpretations. Time-resolved spectral measurements show a high sensitivity to the actual drive intensity on target. Time-resolved spectral measurements are particularly important for determining the hydrodynamic wave timing in the ignition-scaled experiments with complex pulse shapes presently carried out on OMEGA.
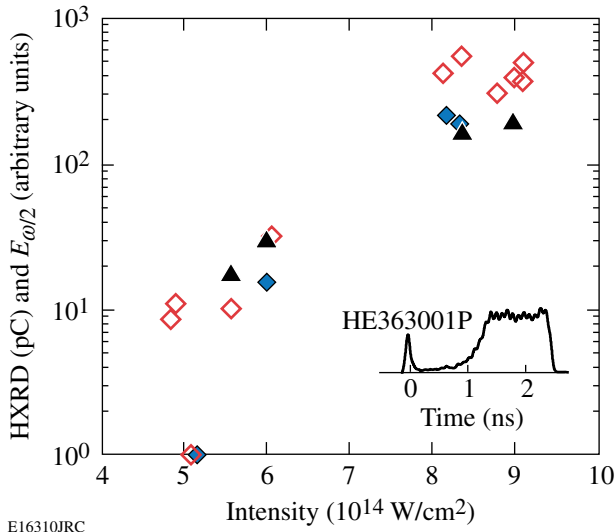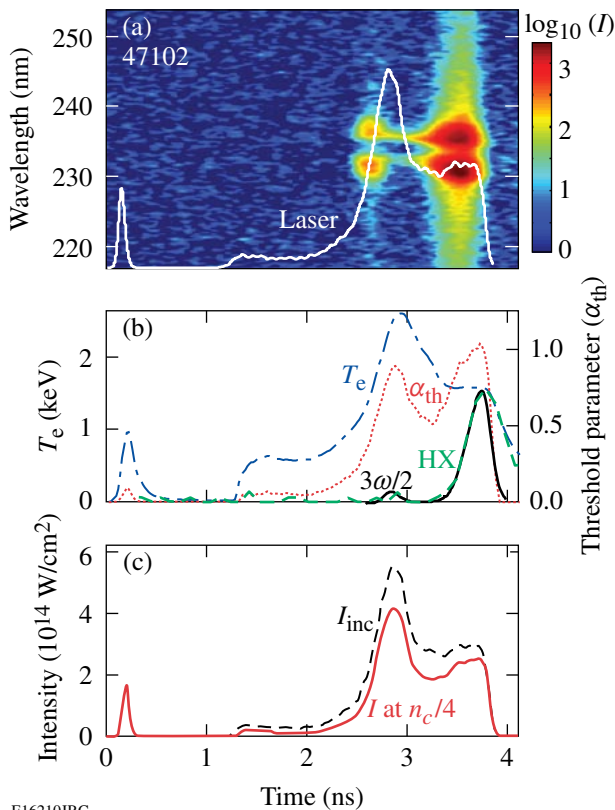
Figure 113.45

Intensity scaling of hard x rays (open and solid diamonds, $h\nu_x > 40$ keV) and the half-harmonic emission (solid triangles) for cryogenic shots with pulse shapes as shown in the insert. The targets were 10-μm CH or CD shells with a 95-μm D_2- or DT-ice layer. Shots with pure CD or CH shells are shown as open diamonds; those with Si-doped outer layers (5 μm) are shown as solid diamonds.

Figure 113.46

Spectrum of the 3/2-harmonic emission (a) from a cryogenic target (4.5-μm CH shell and 95-μm D_2 ice layer) imploded with 11.7 kJ of laser energy and full beam smoothing (DPP, PS, and 1-THz SSD bandwidth). *LILAC* predictions for T_e and α_{th} are shown in (b). Also, shown in (b) are the normalized 3/2-harmonic and hard x-ray powers. (The extended hard x-ray emission is an artifact of the cryogenic target implosion and does not relate to extended fast electron production.) In (c) the incident intensity and the intensity at $n_c/4$ are shown. The thin CH shell burns through at ~3.2 ns.

Discrepancies between the hydrodynamic predictions and experimental scattered-light data as shown in Fig. 113.37(b) are common. The initial spike of the incident laser pulse is typically more strongly absorbed than predicted by simulations using standard flux-limited electron-heat transport [dashed–dotted line in Fig. 113.37(b)]. In contrast, the *LILAC* prediction using nonlinear electron-heat transport is in excellent agreement for the scattered light of the initial spike. At later times (between 2 and 3 ns in Fig. 113.37) the experimental data tend to be predicted better using flux-limited electron transport. Both transport models consistently predict less scattered light than is observed.

The scattered-light spectra (Figs. 113.36, 113.37, 113.39, 113.42, and 113.43) contain a wealth of information about the plasma evolution and the laser–plasma interaction processes. Refraction in the plasma deflects part of all 60 beams of OMEGA into the collection optics as shown schematically in Fig. 113.38. The exact contribution of any beam varies in time and with the position of the beam relative to the collection optics. This is simulated numerically with a ray-trace code using the time-varying plasma profiles obtained from one-dimensional *LILAC* simulations.[40] These simulations show that the rapid blue shift during the initial irradiation of the target is due to the buildup of plasma[36] that occurs when the optical path length traversed by the scattered light decreases rapidly with time, since the index of refraction in the plasma is $\mu = \left(1 - n_e/n_c\right)^{1/2} < 1$, where n_e and n_c are the electron density and critical electron density. These ray-trace simulations show that the scattered light shifts to the blue whenever the mass ablation rate increases.

The remarkable sensitivity of the scattered-light spectra on the electron-heat-transport model used in the hydrodynamic simulations is shown in Fig. 113.39. For this narrowband shot (no SSD bandwidth) we note that the simulations reproduce both the refracted spectrum and the "blow-by" spectrum (the

small part of the laser beam opposing the FABS that misses the target entirely and is seen only when viewing the target through one of the focusing lenses). The experimental spectrum [Fig. 113.39(a)] is better (though not perfectly) matched by the simulations using nonlocal electron-heat transport [Fig. 113.39(b)] than by the standard flux-limited heat transport with $f = 0.06$ [Fig. 113.39(c)]. Figure 113.40 also shows much better agreement between observed and simulated scattered-light power with the nonlocal heat-transport model. The improved predictability of the hydrodynamic simulations for picket pulses is evident in the time-integrated absorption fractions for the 200-ps experiments shown in Fig. 113.41.

Obtaining accurate hydrodynamic simulations of these short-pulse experiments is crucial since the initial spikes in these ignition-relevant pulse shapes (Figs. 113.37, 113.42, 113.45, and 113.46) are intended to shape the adiabat of the implosion.[10]

The scattered laser power is generally underpredicted by *LILAC* during the main part of the laser pulse (see Figs. 113.37, 113.42, and 113.43). The scattered-light spectrum in Fig. 113.42 (20-μm CH shell, 1-ns square pulse, 1-THz SSD) shows a change from the symmetrical, incident SSD spectrum to one that is red peaked (see lineouts in Fig. 113.42). This change is evidence for nonlinear scattering in the plasma corona such as stimulated Brillouin scattering (SBS) with a strong electromagnetic (EM) seed.[15] Intrabeam forward SBS, where scattering of the blue spectrum seeds SBS in the red of the same beam, would be expected to give rise to a red-peaked spectrum with negligible net energy loss. In contrast, cross-beam energy transfer has been shown in planar geometry to be very effective[15,41] and can lead to significant loss of drive energy. The effects seen in spherical geometry are difficult to reproduce in planar geometry with its restricted number of beam angles. The multitude of contributing beams and varying beam paths render it difficult to numerically model these effects in spherical geometry. The enhanced scattering at later times tends to be less detrimental to a low-adiabat implosion than the increased absorption during the early phase of plasma formation that is better modeled using the nonlocal model.

The potential significance of the cross-beam energy transfer is seen in Fig. 113.43 for an implosion experiment without SSD bandwidth. The scattered light during the picket is well reproduced in spectrum and power by the simulations using nonlocal transport. In contrast, significant differences are observed between the experimental and simulated spectra and powers starting with the intensity rise to the main pulse. The simulated spectrum predicts a larger blue shift than is observed.

As mentioned previously, ray-trace simulations indicate that an increasing mass ablation rate leads to an increasing blue shift. The observed time-resolved spectrum in Fig. 113.43 indicates that there is less drive pressure at the onset of the main pulse than predicted, consistent with the observed increased scattered-light power at that time. The simulated spectrum in Fig. 113.43 between 2 and 3.3 ns shows two strongly red-shifted components not seen in the experimental data. These components are due to light rays with the closest approach to the critical surface; they also are the most intense rays in each beam and provide the most efficient drive. It is plausible that their absence indicates a loss due to cross-beam energy transfer. (Increased absorption for these rays could explain the absence of these red components but would be inconsistent with the reduced drive deduced from the reduced blue shift of the spectrum and the observed increased scattered-light power.) It should be noted that these detailed features of the spectra are only visible without SSD bandwidth as a 1-THz SSD bandwidth completely washes out these details.

The scattered-light spectra at various wavelengths are shown in Fig. 113.44 for a room-temperature, low-adiabat ($\alpha = 3$), narrowband (no SSD bandwidth) implosion. The outer 5 μm of this target are doped with 6% atomic Si in an effort to reduce hard x-ray production. Figures 113.44(a)–113.44(c) show the spectra and powers of the scattered light near the incident laser wavelength and the odd-integer half-harmonics. The wavelength scales of the $\omega/2$ and $3\omega/2$ spectra are chosen to have equal frequency scales. The existence of these odd-integer half-harmonic spectra is compelling evidence for the TPD instability,[2,13] while the separation of the two peaks reflects the different secondary scattering processes involved.[42]

The half-harmonic spectrum in Fig. 113.44(c) is consistent with plasmon-to-photon mode conversion[42] analogous to the conversion process underlying resonance absorption.[43] The red component of this spectrum is stronger since the lower-frequency TPD plasmon can convert near the point of its creation while the higher-frequency (blue) plasmon has to propagate to its turning point before conversion. The spectral splitting is consistent with linear TPD theory.[38]

The 3/2-harmonic emission [Fig. 113.44(b)] is due to Thomson scattering of incident photons off TPD plasmons. In spherical geometry, the relevant phase-matching conditions are easily satisfied due to the large number of available probe rays for Thomson scattering. This explains why the blue peak of the 3/2-harmonic spectrum tends to be more intense than the red peak since the phase-matching conditions

can be satisfied for the blue plasmon at its point of creation. For the red 3/2-harmonic component, the phase-matching conditions require that the red plasmon propagate down the density gradient and acquire the requisite k-vector length for Thomson scattering.[42]

Given these differences in the generation processes for the odd-integer half-harmonic emissions, it is surprising that their power histories are nearly identical, as seen in Fig. 113.44(d). It is equally surprising that the temporal hard x-ray emission follows the half-harmonic emission as shown in Fig. 113.44(d). This is probably a consequence of the extremely rapid growth of the TPD instability, which is followed by saturation.

The exponential scaling of the hard x-ray and half-harmonic emission with laser intensity is shown in Fig. 113.45. This kind of scaling is observed only if the target and pulse shapes are kept constant while the intensity alone is varied. Changing either the pulse shape or the target causes the simple scaling to break down. In particular, doping the outer layers of the target with high-Z elements (Si or Ge) reduces the hard x-ray emission while affecting the half-harmonics to a lesser extent.[44] The underlying cause for these changes can be partly attributed to changes in density scale length, electron temperature, and absorption of the incident light on the way to $n_c/4$. However, a Z-dependence in the saturation mechanisms for the TPD instability cannot be ruled out.

The TPD threshold (and presumably also its saturation) dependence on density scale length, electron temperature, and intensity is illustrated in Fig. 113.46. The 3/2-harmonic emission has an initial, weak burst at 2.8 ns before the peak of the laser pulse. Its main emission occurs at the end of the laser pulse when the laser intensity is only half of its peak value but the threshold parameter α_{th} is highest due to the reduced temperature. The fast-electron production also peaks at that time as indicated in Fig. 113.46(b). [The extended hard x-ray signal observed in Fig. 113.46(b) is consistently observed in cryogenic shots and is tentatively attributed to energetic electrons striking surfaces in the vicinity of the target that are present only during cryogenic shots.] As in room-temperature targets, the strong half-integer harmonic emission generally correlates well with the hard x-ray emission temporally. Weaker precursor half-integer harmonic emission is typically not reflected in the hard x-ray signals.

The threshold parameter α_{th} represents a simplified view of the actual experimental conditions, yet it appears to give useful insight into the threshold behavior (and possibly also its saturation behavior) of this instability. This instability is as ubiquitous for direct-drive laser-fusion experiments as it is intractable theoretically, particularly with regard to its ramifications of fast-electron generation and fast-electron preheat.

Conclusions

The spectra and powers of the scattered laser light during direct-drive ICF implosion experiments on OMEGA have been shown to be powerful tools for fine-tuning hydrodynamic code simulations and identifying laser–plasma interaction processes. Short pulses frequently precede the main laser pulse for adiabat shaping of the implosion. These pulses have been shown experimentally to have higher absorption than predicted by hydrodynamic code simulations using flux-limited diffusion. Comparisons of *LILAC* simulations with these experimental data have led to an improved nonlocal electron-transport model.

Later during target irradiation the scattered-light spectra and powers indicate the presence of enhanced scattering that reduces the laser drive of the target. The scattered-light spectra point to a nonlinear interaction process that is tentatively identified as EM-seeded SBS. The EM seed here is provided by the scattered light of any of the 60 beams of OMEGA and the required SBS gain is small. The spectra indicate that the increase in mass ablation during the rise of the main pulse is not as large as predicted by hydrodynamic simulations, supporting the reduced laser–plasma coupling observed in the power measurements.

The presence of the TPD instability is clearly seen in these direct-drive-implosion experiments through the emission of $\omega/2$ and $3\omega/2$ light as well as hard x rays above 50 keV. The sensitivity of the TPD instability to laser intensity, density-gradient scale lengths, and electron temperature has been identified using complex pulse shapes. Although there is no easily applicable theory for interpreting the details of the observation, the data obtained so far permit tailoring implosion experiments to minimize the detrimental effects of the energetic electron production associated with the TPD. In particular, doping of the outer plastic layers of the target with high-Z elements appears to mitigate hard x-ray production although the detailed mechanism is not well understood at present.

REFERENCES

1. R. S. Craxton and R. L. McCrory, Laboratory for Laser Energetics, University of Rochester, Rochester, NY, LLE Report No. 108 (1980).

2. M. C. Richardson, R. S. Craxton, J. Delettrez, R. L. Keck, R. L. McCrory, W. Seka, and J. M. Soures, Phys. Rev. Lett. **54**, 1656 (1985).

3. R. Cauble and W. Rozmus, Phys. Fluids **28**, 3387 (1985).

4. W. Seka, C. Stoeckl, V. N. Goncharov, R. E. Bahr, T. C. Sangster, R. S. Craxton, J. A. Delettrez, A. V. Maximov, J. Myatt, A. Simon, and R. W. Short, Bull. Am. Phys. Soc. **49**, 179 (2004).

5. P. W. McKenty, J. A. Marozas, V. N. Goncharov, K. S. Anderson, R. Betti, D. D. Meyerhofer, P. B. Radha, T. C. Sangster, S. Skupsky, and R. L. McCrory, Bull. Am. Phys. Soc. **51**, 295 (2006).

6. P. W. McKenty, T. C. Sangster, M. Alexander, R. Betti, R. S. Craxton, J. A. Delettrez, L. Elasky, R. Epstein, A. Frank, V. Yu. Glebov, V. N. Goncharov, D. R. Harding, S. Jin, J. P. Knauer, R. L. Keck, S. J. Loucks, L. D. Lund, R. L. McCrory, F. J. Marshall, D. D. Meyerhofer, S. P. Regan, P. B. Radha, S. Roberts, W. Seka, S. Skupsky, V. A. Smalyuk, J. M. Soures, K. A. Thorp, M. Wozniak, J. A. Frenje, C. K. Li, R. D. Petrasso, F. H. Séguin, K. A. Fletcher, S. Padalino, C. Freeman, N. Izumi, J. A. Koch, R. A. Lerche, M. J. Moran, T. W. Phillips, G. J. Schmid, and C. Sorce, Phys. Plasmas **11**, 2790 (2004).

7. V. N. Goncharov, P. McKenty, S. Skupsky, R. Betti, R. L. McCrory, and C. Cherfils-Clérouin, Phys. Plasmas **7**, 5118 (2000).

8. R. L. McCrory, R. E. Bahr, T. R. Boehly, T. J. B. Collins, R. S. Craxton, J. A. Delettrez, W. R. Donaldson, R. Epstein, V. N. Goncharov, R. Q. Gram, D. R. Harding, P. A. Jaanimagi, R. L. Keck, J. P. Knauer, S. J. Loucks, F. J. Marshall, P. W. McKenty, D. D. Meyerhofer, S. F. B. Morse, O. V. Gotchev, P. B. Radha, S. P. Regan, W. Seka, S. Skupsky, V. A. Smalyuk, J. M. Soures, C. Stoeckl, R. P. J. Town, M. D. Wittman, B. Yaakobi, J. D. Zuegel, R. D. Petrasso, D. G. Hicks, and C. K. Li, in *Inertial Fusion Sciences and Applications 99*, edited by C. Labaune, W. J. Hogan, and K. A. Tanaka (Elsevier, Paris, 2000), pp. 43–53.

9. S. Skupsky, R. Betti, T. J. B. Collins, V. N. Goncharov, D. R. Harding, R. L. McCrory, P. W. McKenty, D. D. Meyerhofer, and R. P. J. Town, in *Inertial Fusion Sciences and Applications 2001*, edited by K. Tanaka, D. D. Meyerhofer, and J. Meyer-ter-Vehn (Elsevier, Paris, 2002), pp. 240–245.

10. V. N. Goncharov, J. P. Knauer, P. W. McKenty, P. B. Radha, T. C. Sangster, S. Skupsky, R. Betti, R. L. McCrory, and D. D. Meyerhofer, Phys. Plasmas **10**, 1906 (2003).

11. R. Betti, K. Anderson, T. R. Boehly, T. J. B. Collins, R. S. Craxton, J. A. Delettrez, D. H. Edgell, R. Epstein, V. Yu. Glebov, V. N. Goncharov, D. R. Harding, R. L. Keck, J. H. Kelly, J. P. Knauer, S. J. Loucks, J. A. Marozas, F. J. Marshall, A. V. Maximov, D. N. Maywar, R. L. McCrory, P. W. McKenty, D. D. Meyerhofer, J. Myatt, P. B. Radha, S. P. Regan, C. Ren, T. C. Sangster, W. Seka, S. Skupsky, A. A. Solodov, V. A. Smalyuk, J. M. Soures, C. Stoeckl, W. Theobald, B. Yaakobi, C. Zhou, J. D. Zuegel, J. A. Frenje, C. K. Li, R. D. Petrasso, and F. H. Séguin, Plasma Phys. Control. Fusion **48**, B153 (2006).

12. S. E. Bodner, D. G. Colombant, J. H. Gardner, R. H. Lehmberg, S. P. Obenschain, L. Phillips, A. J. Schmitt, J. D. Sethian, R. L. McCrory, W. Seka, C. P. Verdon, J. P. Knauer, B. B. Afeyan, and H. T. Powell, Phys. Plasmas **5**, 1901 (1998); J. Myatt, A. V. Maximov, W. Seka, R. S. Craxton, and R. W. Short, Phys. Plasmas **11**, 3394 (2004).

13. W. Seka, R. S. Craxton, R. E. Bahr, D. L. Brown, D. K. Bradley, P. A. Jaanimagi, B. Yaakobi, and R. Epstein, Phys. Fluids B **4**, 432 (1992).

14. W. Seka, R. S. Craxton, R. Bahr, D. Bradley, P. Jaanimagi, J. Knauer, S. Letzring, D. Meyerhofer, R. L. Short, A. Simon, and J. M. Soures, Bull. Am. Phys. Soc. **35**, 1944 (1990).

15. W. Seka, H. A. Baldis, J. Fuchs, S. P. Regan, D. D. Meyerhofer, C. Stoeckl, B. Yaakobi, R. S. Craxton, and R. W. Short, Phys. Rev. Lett. **89**, 175002 (2002).

16. W. Seka, R. E. Bahr, R. W. Short, A. Simon, R. S. Craxton, D. S. Montgomery, and A. E. Rubenchik, Phys. Fluids B **4**, 2232 (1992).

17. J. M. Soures, T. C. Bristow, H. Deckman, J. Delettrez, A. Entenberg, W. Friedman, J. Forsyth, Y. Gazit, G. Halpern, F. Kalk, S. Letzring, R. McCrory, D. Peiffer, J. Rizzo, W. Seka, S. Skupsky, E. Thorsos, B. Yaakobi, and T. Yamanaka, in *Laser Interaction and Related Plasma Phenomena*, edited by H. J. Schwarz, H. Hora, M. J. Lubin, and B. Yaakobi (Plenum Press, New York, 1981), Vol. 5, pp. 463–481.

18. W. Seka, R. S. Craxton, J. Delettrez, L. Goldman, R. Keck, R. L. McCrory, D. Shvarts, J. M. Soures, and R. Boni, Opt. Commun. **40**, 437 (1982).

19. W. Seka, L. M. Goldman, M. C. Richardson, J. M. Soures, K. Tanaka, B. Yaakobi, R. S. Craxton, R. L. McCrory, R. Short, E. A. Williams, T. Boehly, R. Keck, and R. Boni, in *Plasma Physics and Controlled Nuclear Fusion Research 1982* (IAEA, Vienna, 1983), Vol. I, pp. 131–137.

20. C. Garban-Labaune *et al.*, Phys. Fluids **28**, 2580 (1985).

21. S. P. Regan, H. Sawada, D. Li, V. N. Goncharov, R. Epstein, J. A. Delettrez, J. P. Knauer, J. A. Marozas, F. J. Marshall, R. L. McCrory, P. W. McKenty, D. D. Meyerhofer, P. B. Radha, W. Seka, T. C. Sangster, S. Skupsky, V. A. Smalyuk, R. Mancini, S. H. Glenzer, O. Landen, and G. Gregori, Bull. Am. Phys. Soc. **51**, 254 (2006).

22. T. R. Boehly, R. S. Craxton, T. H. Hinterman, P. A. Jaanimagi, R. L. Keck, J. H. Kelly, T. J. Kessler, R. L. Kremens, S. A. Kumpan, S. A. Letzring, R. L. McCrory, S. F. B. Morse, W. Seka, S. Skupsky, J. M. Soures, and C. P. Verdon, in *Proceedings of the IAEA Technical Committee Meeting on Drivers for Inertial Confinement Fusion*, edited by J. Coutant (IAEA, Vienna, 1995), pp. 79–86.

23. Kato *et al.*, Phys. Rev. Lett. **53**, 1057 (1984).

24. T. J. Kessler, Y. Lin, J. J. Armstrong, and B. Velazquez, in *Laser Coherence Control: Technology and Applications*, edited by H. T. Powell and T. J. Kessler (SPIE, Bellingham, WA, 1993), Vol. 1870, pp. 95–104.

25. T. J. Kessler, Y. Lin, L. S. Iwan, W. P. Castle, C. Kellogg, J. Barone, E. Kowaluk, A. W. Schmid, K. L. Marshall, D. J. Smith, A. L. Rigatti, J. Warner, and A. R. Staley, in *Second Annual International Conference Solid State Lasers for Application to Inertial Confinement Fusion*, edited by M. L. André (SPIE, Bellingham, WA, 1997), Vol. 3047, pp. 272–281.

26. J. E. Rothenberg, J. Appl. Phys. **87**, 3654 (2000).

27. S. Skupsky, R. W. Short, T. Kessler, R. S. Craxton, S. Letzring, and J. M. Soures, J. Appl. Phys. **66**, 3456 (1989).

28. D. R. Harding, D. D. Meyerhofer, S. J. Loucks, L. D. Lund, R. Janezic, L. M. Elasky, T. H. Hinterman, D. H. Edgell, W. Seka, M. D. Wittman, R. Q. Gram, D. Jacobs-Perkins, R. Early, T. Duffy, and M. J. Bonino, Phys. Plasmas **13**, 056316 (2006).

29. D. H. Edgell, W. Seka, R. S. Craxton, L. M. Elasky, D. R. Harding, R. L. Keck, and M. D. Wittman, Fusion Sci. Technol. **49**, 616 (2006).

30. D. H. Edgell, W. Seka, R. S. Craxton, L. M. Elasky, D. R. Harding, R. L. Keck, L. D. Lund, and M. D. Wittman, J. Phys. IV France **133**, 903 (2006).

31. W. Seka, V. N. Goncharov, J. A. Delettrez, D. H. Edgell, I. V. Igumenshchev, R. W. Short, A. V. Maximov, J. Myatt, and R. S. Craxton, Bull. Am. Phys. Soc. **51**, 340 (2006).

32. J. Delettrez, R. Epstein, M. C. Richardson, P. A. Jaanimagi, and B. L. Henke, Phys. Rev. A **36**, 3926 (1987).

33. R. C. Malone, R. L. McCrory, and R. L. Morse, Phys. Rev. Lett. **34**, 721 (1975).

34. V. N. Goncharov, T. C. Sangster, P. B. Radha, T. R. Boehly, T. J. B. Collins, R. S. Craxton, J. A. Delettrez, R. Epstein, V. Yu. Glebov, S. X. Hu, I. V. Igumenshchev, R. Janezic, S. J. Loucks, J. R. Marciante, J. A. Marozas, F. J. Marshall, D. N. Maywar, J. P. Knauer, P. W. McKenty, S. P. Regan, R. G. Roides, W. Seka, S. Skupsky, V. A. Smalyuk, J. M. Soures, C. Stoeckl, R. Betti, R. L. McCrory, D. D. Meyerhofer, D. Shvarts, J. A. Frenje, R. D. Petrasso, and C. K. Li, "Performance of Direct-Drive Cryogenic Targets on OMEGA," to be published Physics of Plasmas (invited).

35. V. N. Goncharov, O. V. Gotchev, E. Vianello, T. R. Boehly, J. P. Knauer, P. W. McKenty, P. B. Radha, S. P. Regan, T. C. Sangster, S. Skupsky, V. A. Smalyuk, R. Betti, R. L. McCrory, D. D. Meyerhofer, and C. Cherfils-Clérouin, Phys. Plasmas **13**, 012702 (2006).

36. T. Dewandre, J. R. Albritton, and E. A. Williams, Phys. Fluids **24**, 528 (1981).

37. W. L. Kruer, *The Physics of Laser–Plasma Interactions*, Frontiers in Physics, Vol. 73, edited by D. Pines (Addison-Wesley, Redwood City, CA, 1988), Chap. 4, pp. 37–43.

38. A. Simon, R. W. Short, E. A. Williams, and T. Dewandre, Phys. Fluids **26**, 3107 (1983).

39. A. L. Richard, J. P. Jadaud, N. Dague, M. C. Monteil, R. E. Turner, D. Bradley, R. J. Wallace, O. L. Landen, J. M. Soures, S. Morse, and G. Pien, in *ECLIM 2000: 26th European Conference on Laser Interaction with Matter*, edited by M. Kálal, K. Rohlena, and M. Šinor (SPIE, Bellingham, WA, 2001), Vol. 4424, pp. 23–26.

40. D. Edgell, W. Seka, J. A. Delettrez, R. S. Craxton, V. N. Goncharov, I. V. Igumenshchev, J. Myatt, A. V. Maximov, R. W. Short, T. C. Sangster, and R. E. Bahr, Bull. Am. Phys. Soc. **52**, 195 (2007).

41. R. K. Kirkwood, J. D. Moody, A. B. Langdon, B. I. Cohen, E. A. Williams, M. R. Dorr, J. A. Hittinger, R. Berger, P. E. Young, L. J. Suter, L. Divol, S. H. Glenzer, O. L. Landen, and W. Seka, Phys. Rev. Lett. **89**, 215003 (2002).

42. R. L. Berger and L. V. Powers, Phys. Fluids **28**, 2895 (1985).

43. W. L. Kruer, in *Laser Plasma Interactions*, edited by R. A. Cairns and J. J. Sanderson (Scottish Universites Summer School in Physics, Edinburgh, Scotland, 1980), pp. 387–432.

44. P. B. Radha, J. P. Knauer, T. C. Sangster, V. N. Goncharov, I. V. Igumenshchev, R. Betti, R. Epstein, D. D. Meyerhofer, and S. Skupsky, Bull. Am. Phys. Soc. **52**, 143 (2007); J. P. Knauer, P. B. Radha, V. N. Goncharov, I. V. Igumenshchev, R. Betti, R. Epstein, F. J. Marshall, S. P. Regan, V. A. Smalyuk, D. D. Meyerhofer, and S. Skupsky, Bull. Am. Phys. Soc. **52**, 233 (2007).